Contributed paper

OPTO-ELECTRONICS REVIEW **8**(3), 251–262 (2000)

Photoelectric properties of HgMnTe photodiodes with ion etched p–n junctions

L.A. KOSYACHENKO[1*], I.M. RARENKO[1], S. WEIGUO[2], L. ZENGXIONG[2], and G. QIBING[2]

[1]Chernovtsy University, 2 Kotsyubinsky Str., 274012 Chernovtsy, Ukraine
[2]Optoelectronics Institute, PO Box 030, 471009 Luoyang, Henan, P.R. China

Photodiodes with p–n junctions formed by ion etching of p-$Hg_{1-x}Mn_xTe$ ($x \approx 0.1$) are reported. The multielement photodiode arrays for mid-infrared region were fabricated using surface passivation, photolithography and three-layer metallisation processes. The absorption curves of the crystals found from optical measurements are treated within the Kane theory for semiconductors with highly nonparabolic energy bands. The parameters of the diodes are obtained from their electrical study. It is shown that due to strong degeneracy of the n^+-layer the $Hg_{1-x}Mn_xTe$ diode structure can be considered as one-sided abrupt n^+-p junction with the barrier height larger significantly than the semiconductor bandgap. The diode responsivity spectra are interpreted in the framework of model taking into account the generation of photocarriers in n^+- and p-regions as well as in the depletion layer. The diode photoresponsivity in the region of the photon energies below semiconductor bandgap is shown to be caused by the gentle slope of the observed absorption edge. Temperature measurements reveal essential peculiarities of carrier tunnelling in the diodes. Invoking the general expression for the tunnelling probability and taking into consideration the opposing flow of electrons allow the observed tunnelling decay at low reverse biases to be explained. The zero bias resistance-area product (R_oA) for the $Hg_{1-x}Mn_xTe$ diodes with cutoff wavelengths 7–8 and 10–11 μm amount up to 20–30 and ~500 Ω cm², respectively, indicating the photodiodes under study to be competitive with $Hg_{1-x}Cd_xTe$ photovoltaic detectors.

Keywords: infrared detectors, HgMnTe photodiodes, R_oA product, photoelectric properties.

1. Introduction

As early as the 1960s, $Hg_{1-x}Mn_xTe$ alloy has been known as an interesting semimagnetic semiconductor (see, for example Ref. 1), and during the last 10–15 years, the $Hg_{1-x}Mn_xTe$ with x = 0.1 is considered as a promising material for mid-infrared applications [2–7]. This semiconductor is attractive primarily due to higher mechanical strength and thermal stability relative to $Hg_{1-x}Cd_xTe$. Electrical, optical, and other properties of $Hg_{1-x}Cd_xTe$ and $Hg_{1-x}Mn_xTe$ at zero magnetic field turn out to be closely similar. To produce p–n junction, techniques used for manufacturing of $Hg_{1-x}Cd_xTe$ photovoltaic detectors (diffusion and ion implantation in particular) were successfully extended to $Hg_{1-x}Mn_xTe$ [4,5,7,8]. As to the $Hg_{1-x}Mn_xTe$ diodes, their main electrical and photoelectric characteristics are comparable to those of $Hg_{1-x}Cd_xTe$ diodes as well.

Theoretical analysis has shown that the $Hg_{1-x}Mn_xTe$ photodiode performance is quite attainable for a practical implementation [8,9]. However, against the backgrounds of the detailed theoretical consideration, experimental studies of the $Hg_{1-x}Mn_xTe$ photodiodes seem to be inadequate: only a few papers on this subject have been published [4,5,7]. This study presents the mid-infrared $Hg_{1-x}Mn_xTe$ photodiodes with p–n junctions formed by ion etching (ion beam milling), the technique borrowed from $Hg_{1-x}Cd_xTe$ technology [10,11]. The paper is primarily devoted to the diode photoelectric properties, particularly spectral responsivity and detectivity. Their interpretation, however, is impossible without determining the optical absorption characteristics of the material, the diode energy diagram and parameters that are also presented in the paper.

2. Photodiode fabrication procedure

For photodiode fabrication, the $Hg_{1-x}Mn_xTe$ ($x \approx 0.1$) single crystals grown by a modified Bridgman technique were used [12]. As-grown crystals were p–type with a hole concentration found from Hall measurements as high as ~10^{17} cm^{-3}. To reduce the hole concentration and to improve the crystal uniformity, the low-temperature annealing was carried out in a closed avacuated quartz ampoules at 200–300°C for a few weeks. The $Hg_{1-x}Mn_xTe$ wafers with the hole concentration $p = (2–5)\times10^{16}$ cm^{-3} were selected for the photodiodes studied.

After mechanical and chemical treatment of the $Hg_{1-x}Mn_xTe$ wafers, standard photolithography methods with photoresist as a protection coating were used to define the active area of the photodiodes. A low-energy ion bombardment, the technique usually applied for ion etching in

*e-mail: oe-dept@phys.chsu.cv.ua

microelectronics technology, was carried out to form a thin n–type layer (~1 μm) on the p–type substrates. The ion bombardment were performed in a common ion etch system generated a highly collimated argon beam of 500–1000 eV energy and 0.5–1 mA/cm^2 current density.

For minimising the surface leakage currents and reducing the density of slow trapping states, an anodic fluoride layer (0.01–0.03 μm) was grown on $Hg_{1-x}Mn_xTe$ from non-aquaous solution of NH_4F in ethylene glycol in electrochemical cell with a platinum electrode. As X-ray photoelectron spectroscopy analysis shown, the main part of the anodic layer is a mixture of mercury, manganese and tellurium fluorides [13]. Constant current density of 0.6–3.0 mA/cm^2 was employed thus resulting in continuous, non-porous and reproducible passivation layers. An additional ZnS film (~0.3 μm) fulfilling the function of both protection and antireflection coating was deposited using vacuum evaporating system. The use of anodic fluoride followed by ZnS deposition provides proper protection of $Hg_{1-x}Mn_xTe$ (preventing the Hg loss from the surface, in particular).

To open the contact windows on p- and n-regions of the diode structure, photolithography methods and special masks were used. The palladium plating process was performed to form the ohmic contact and next Cr film (~0.05 μm) was evaporated to obtain an interface suitable for adhesion with ZnS. Finally, Au layer (~1 μm) was deposited for good connection to electrodes with gold wire bounder.

The above fabricating technologies have been used for realising planar and mesa multielement photodiode arrays with sensitive area of element 50×50 μm (or other sizes). The schematic cross section of the $Hg_{1-x}Mn_xTe$ photodiode structures are shown in Fig. 1.

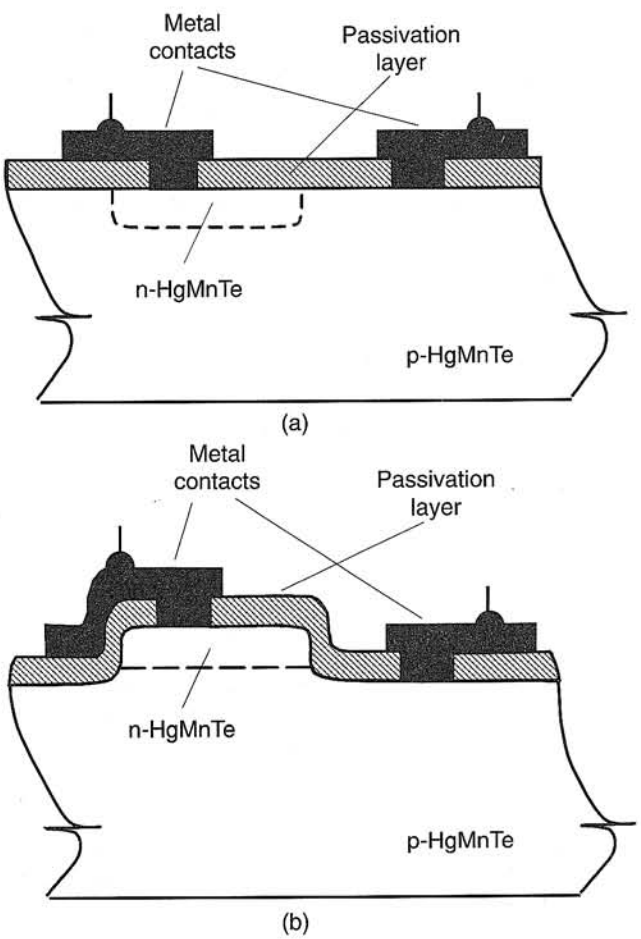

Fig. 1. Cross-section of planar (a) and meza (b) $Hg_{1-x}Mn_xTe$ photodiode elements.

3. Optical absorption in $Hg_{1-x}Mn_xTe$ crystals

In order the photoelectric characteristics of a diode to be interpreted, the optical absorption spectra of the material is required to know in a wide spectral range for interband electron transitions.

The spectral dependence of the absorption coefficient was found from the transmission curves of the $Hg_{1-x}Mn_xTe$ wafers used for diode fabrication [14]. To increase the accuracy of transmission measurements at higher absorption coefficients, the wafers were polished down to a thickness of about 20 μm. The experimental data obtained were processed with allowance made for multiple reflection in a sample.

Figure 2 shows the absorption curves thus obtained for the $Hg_{0.9}Mn_{0.1}Te$ and $Hg_{0.88}Mn_{0.12}Te$ at 80 K. It is evident that the absorption spectra can be divisible into two regions. In the low-energy region the absorption coefficient only weakly depends on photon energy, whereas in the high-energy region the very strong dependence on hν is observed. There is reason to believe that the former is caused by a free-carrier absorption while the latter is associated with electron interband transitions, i.e., the transitions involved in photogeneration of electron-hole pairs.

To describe the intrinsic absorption in $Hg_{1-x}Mn_xTe$ analytically, one can use the Kane theory well proved for nar-

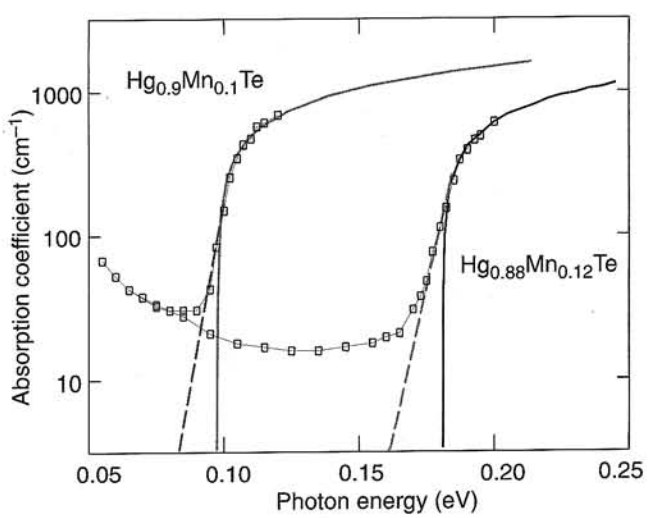

Fig. 2. Optical absorption in $Hg_{0.9}Mn_{0.1}Te$ and $Hg_{0.88}Mn_{0.12}Te$ crystals at 80 K. The squares show experimental data, the solid and dashed curves have been calculated using Eqs. (4) and (7), respectively.

 © 2000 COSiW SEP, Warsaw

row-gap semiconductors with highly nonparabolic energy bands [15]. If the spin-orbit splitting is large enough ($\Delta >> E_g$) and the electron effective mass m_e is much smaller than the hole effective mass m_h, the dispersion law in the conduction band can be presented as

$$E_c(k) = \frac{\hbar^2 k^2}{2m_e} + \frac{1}{2}[\eta(k) - E_g], \tag{1}$$

where $\eta(k)$ is related to the energy band parameter P by the expression

$$\eta = \left(E_g^2 + \frac{8}{3}p^2k^2\right)^{1/2}. \tag{2}$$

The wave number k appearing in Eqs. (1) and (2) is a solution of the equation

$$h\nu = E_c(k) + E_v(k) + E_g, \tag{3}$$

with the E-k relationship for the valence band can be considered as a parabolic law, i.e., $E_v(k) = \hbar^2k^2/2m_h$. Within this approximation the absorption coefficient for electron transitions between the heavy-hole band and the conduction band can be written as [16]

$$\alpha(h\nu) = \frac{C}{n_o} A\gamma^2 \frac{m_v}{m_o}\left(\frac{m_o}{m_e}\right)^{1/2} \times \left(\frac{E_g}{h\nu}\right)^{1/2} (h\nu - E_g)^{1/2}, \tag{4}$$

where $C = 3.8\times10^5$ with energies measured in eV and α in cm^{-1}, n_o is the refractive index, $m_v = m_o m_h/(m_o+m_h)$, $\gamma = (1/2)(1 + E_g/\eta)$, $A = (2h\nu - E_g)(2h\nu + m_v E_g/m_o)$ (m_o being the free-space electron mass). Hence, determining E_g from the measured absorption edge (Fig. 2) and using for $Hg_{1-x}Mn_xTe$ the "standard" relationships [8]

$$m_e = 5.7\times10^{-16} E_g m_o/P^2, \quad m_h = 0.5\, m_o, \tag{5}$$

$$P = (6.461 - 0.121x)\times10^{-8}\ eVcm \tag{6}$$

an absorption curve can be found from Eq. (4) using Eqs. (1), (2), and (3). The results thus obtained for $Hg_{0.9}Mn_{0.1}Te$ and $Hg_{0.88}Mn_{0.12}Te$ are shown in Fig. 2 as solid lines. The computed curves are matched with the experimental data points by adjusting the C value in Eq. (4). It should be noted that in the $\alpha < 1000\ cm^{-1}$ region Eq. (4) is reduced to the well-known square-root law $\alpha \sim (h\nu - E_g)^{1/2}$ [14].

As it can be seen in Fig. 2, good agreement between theory and experiment is observed in the region of large absorption coefficient. In the $\alpha < 100$–$200\ cm^{-1}$ region the experimental points on the edges of the absorption curves run considerably above the calculated values. It is generally believed that the gentle slope of the intrinsic absorption edge observed in a number of compound semiconductors is caused by microfluctuations and inclusions with different composition of the material [17,18]. For semiconductors similar to $Hg_{1-x}Cd_xTe$ the tail of the absorption edge follows the exponential Urbach law

$$\alpha(h\nu) = \alpha_o \exp\left(\frac{h\nu - E_s}{\sigma_o}\right) = \alpha_{oo} \exp\left(\frac{h\nu}{\sigma_o}\right), \tag{7}$$

where E_s is the energy somewhat smaller than E_g, α_o and $\alpha_{oo} = \alpha_o \exp(-E_g/\sigma_o)$ are the $h\nu$ independent values, and σ_o is the so-called broadening (tailing) parameter, i.e., the energy characterising the compositional fluctuations and inhomogeneities of the material.

It can be seen from Fig. 2 that for the $Hg_{1-x}Mn_xTe$ crystals, Eq. (7) within the absorption edge is really close to the exponential law. Good agreement with the measured absorption curves is achieved when σ_o = 4.2 meV for $Hg_{0.9}Mn_{0.1}Te$ and σ_o = 5.8 meV for $Hg_{0.88}Mn_{0.12}Te$ (Fig. 2, dashed lines). The α_{oo} values were chosen to fit Eq. (7) for the data at α = 500–600 cm^{-1}.

Thus, the absorption curves for the $Hg_{1-x}Mn_xTe$ crystals are governed by Eq. (4) in the region of large absorption coefficient ($h\nu > E_g$) and by Eq. (7) within the tail of the absorption edge ($h\nu < E_g$). Although Eq. (4) has been borne out by experiment only in the region of the measured absorption coefficients less than 700–800 cm^{-1}, the errors associated with the deviation of true values of from theory in the $\alpha > 10^3\ cm^{-1}$ region is of little importance for the diode photoelectric characteristics. As will be shown below, in the high-energy region the absorption coefficient becomes such large that the photoelectric quantum yield saturates, that is, ceases to depend on $h\nu$.

4. Diode energy diagram and parameters

The barrier height, depletion layer width as well as some parameters of n- and p-regions, required to govern the photoelectric properties of the $Hg_{1-x}Mn_xTe$ diode structure, can be found from the electrical measurements.

Figure 3 shows typical I–V characteristics taken from the $Hg_{0.9}Mn_{0.1}Te$ and $Hg_{0.88}Mn_{0.12}Te$ diodes at 80 K. The diodes are evident to have clearly defined rectifying properties. An important point to note here is that in the region of large forward currents the I(V) dependence yields a straight line. This is because the built-in potential, V_{bi}, is almost compensated by the large applied voltage, i.e., one can write $V = V_{bi} + IR_s$, where IR_s is a voltage drop across a series resistance of the substrate R_s. Hence, the cutoff on the V-axis and the slope of the straight-line portion of the measured I–V curve give the built-in potential and the substrate resistance, respectively. Of special interest is that the barrier height in the p–n junction structures studied, $\varphi_o = eV_{bi}$ = 0.24–0.27 eV, is distinctly larger than the semi-

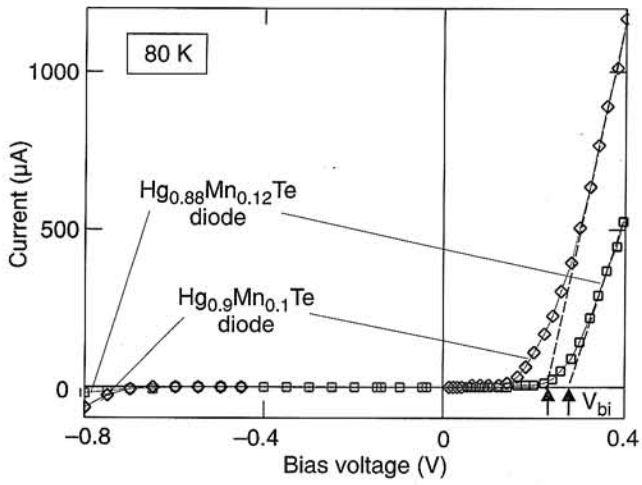

Fig. 3. Current-voltage characteristics for $Hg_{0.9}Mn_{0.1}Te$ and $Hg_{0.88}Mn_{0.12}Te$ photodiodes at 80 K.

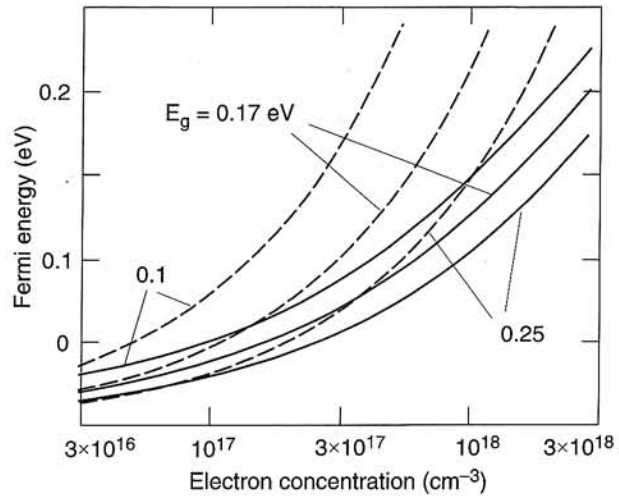

Fig. 4. The Fermi energy as a function of the electron concentration in the conduction band of $Hg_{1-x}Mn_xTe$ for E_g = 0.1, 0.17, and 0.25 eV. The solid and dashed lines correspond to the Kane and parabolic dispersion laws, respectively.

conductor bandgap. Obviously, this is possible only as p- and/or n-regions are degenerated. Being in mind the high doping of the near-surface layer, the degeneracy should be assigned to the n^+-region, particularly in light of the very small electron effective mass in a narrow-gap $Hg_{1-x}Mn_xTe$.

According to the Kane theory [15] in a strongly degenerate n-type semiconductor, the Fermi level enters into the conduction band by the energy given by

$$E_{Fn} = \frac{\hbar^2(3\pi^2 n)^{2/3}}{2m_e} + \frac{1}{2}\left(\sqrt{E_g^2 + \frac{8}{3}P^2(3\pi^2 n)^{2/3}} - E_g\right), \quad (8)$$

where n is the electron concentration, m_e is the electron effective mass and P is the band parameter, defined by Eqs. (5) and (6), respectively.

Figure 4 shows the Fermi energy E_{Fn} as a function of the electron concentration for the Kane model, calculated from Eq. (8), and for the parabolic dispersion law where $E_{Fn} = \hbar^2(3\pi^2 n)^{2/3}/2m_e$. The calculation have been performed for E_g = 0.1, 0.18, and 0.25 eV, i.e., for the cutoff wavelength ~12 μm, ~7 μm, and ~5 μm (the curves are not shown for $n < 3\times10^{16}$ cm^{-3} since Eq. (8) is inapplicable as E_{Fn} is smaller than ~5 kT, 0.035 eV at 80 K). It can be seen from the figure that as the electron concentration ranges within 10^{17}–10^{19} cm^{-3} the Fermi energy achieves the significant values. In this range of n the departure from the parabolic dispersion law must be taken into account, i.e., to obtain the Fermi energy, Eq. (8) should be used (the narrower the bandgap, the larger is the difference between the two approximations). It follows from Fig. 4 that the Fermi energy becomes as large as 0.1–0.2 eV when the electron concentration amounts to $(1–3)\times10^{18}$ cm^{-3}, i.e., the values quite realised in the ion etched p–n junctions.

As to p-region with the hole concentration p = $(2–5)\times10^{16}$ cm^{-3} and the hole effective mass $m_h = 0.5\ m_o$, the valence band may be considered to be nondegenerated. In this case the energy distance from the Fermi level to the top of the valence band, E_{Fp}, can easily be found from the equality

$$p = N_v \exp\left(-\frac{E_{Fp}}{kT}\right) = 2\left(\frac{8\pi^3 kT}{\hbar^2}\right)^{2/3} \exp\left(-\frac{E_{Fp}}{kT}\right), \quad (9)$$

where N_v is the effective density of states in the valence band. It follows from Eq. (9) that for T = 80 K, $m_h = 0.5m_o$ and the p values indicated above $\Delta\mu = kT\ln(N_v/p)$ = 0.022–0.028 eV, i.e., the Fermi level is located well above the top of the valence band. From the above reasoning, we arrive at the energy-band diagram of the $Hg_{1-x}Mn_xTe$ n^+-p junction displayed in Fig. 5. From the figure we have

$$\varphi_o = E_g + E_{Fn} - E_{Fp}, \quad (10)$$

whence $E_{Fn} = \varphi_o - E_g + E_{Fp}$. For the $Hg_{0.9}Mn_{0.1}Te$ and $Hg_{0.88}Mn_{0.12}Te$ diodes φ_o = 0.24 and 0.27 eV (E_g = 0.1 and 0.17 eV) that yields $E_{Fn} \approx$ 0.15 and 0.12 eV, respectively.

On discussing the energy diagram of the $Hg_{1-x}Mn_xTe$ diode structure, it is pertinent to compare its doping profile with that in $Hg_{1-x}Cd_xTe$ p–n junctions. Both ion bombardment and ion implantation of mercury-based materials like $Hg_{1-x}Cd_xTe$ or $Hg_{1-x}Mn_xTe$ are known to create near the surface excess of Hg atoms in the form of interstitials acting as donors. These neutralise Hg vacancies acting as acceptors thus converting p–type material to n–type. At the same time, the Hg excess atoms can diffuse into the bulk also inducing vacancy annihilation and forming a more deep n–layer [10,19,20]. In the case of $Hg_{1-x}Cd_xTe$, the near-surface layer has a thickness of the order of 0.1 μm and a high concentration of electrons whereas in the deep diffusion-induced layer the electron concentration amounts to $(2–5)\times10^{16}$ cm^{-3} and its thickness is much larger than that of the near-surface layer [10].

 © 2000 COSiW SEP, Warsaw

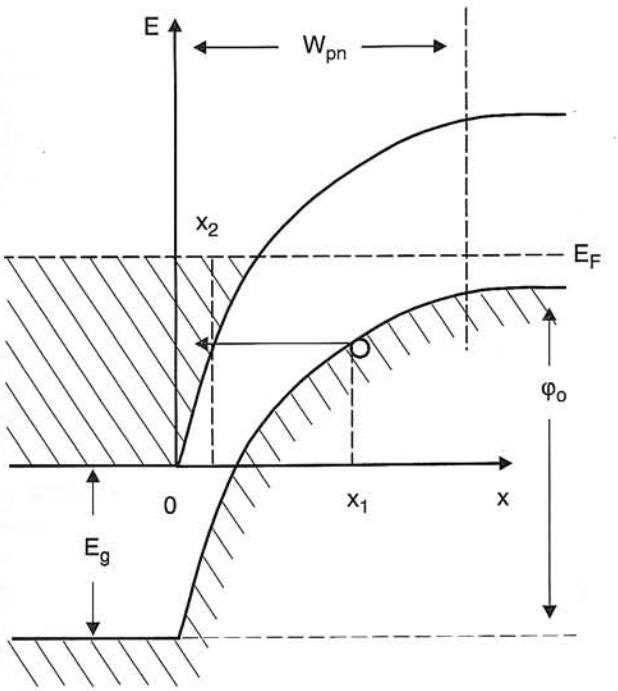

Fig. 5. Energy-band diagram of $Hg_{1-x}Mn_xTe$ n^+-p junction in thermal equilibrium. The arrow indicates interband tunnelling transition.

For $Hg_{1-x}Mn_xTe$, however, it has been found a strong decrease of the mercury diffusion coefficient that reflects the relative stability of the material compared to $Hg_{1-x}Cd_xTe$ [11]. As a result, the thickness of the diffusion-induced layer drastically decreases, i.e., ion bombardment forms the heavily-doped near-surface layer (~1 μm, ~10^{18} cm^{-3}) without an extended intermediate layer of moderate carrier concentration. It is also noteworthy that the observed values of built-in potential (0.24–0.27 V) can be obtained at the boundary between p-region and strongly degenerate n^+-region rather than moderate doped nondegenetare n-region.

Thus, the diode structure under study can be considered as an abrupt one-sided n^+-p junction with the depletion layer located in the relative lightly doped p-region (see Fig. 5). For such kind of the diode structure the depletion layer width is defined by

$$W_{pn} = \sqrt{\frac{2\varepsilon\varepsilon_o(\varphi_o - eV)}{e^2 N_a}}, \qquad (11)$$

where N_a is the concentration of non-compensated acceptors in the substrate, ε_o and ε are the free-space and semiconductor permittivities, respectively (ε = 17.6 for $Hg_{1-x}Mn_xTe$ (x ≈ 0.1) [8]).

5. Spectral responsivity of the diodes

The spectral distribution of photoresponsivity for two diodes on $Hg_{1-x}Mn_xTe$ with x = 0.1 and x = 0.12 obtained using standard measurement technique are shown in Fig. 6.

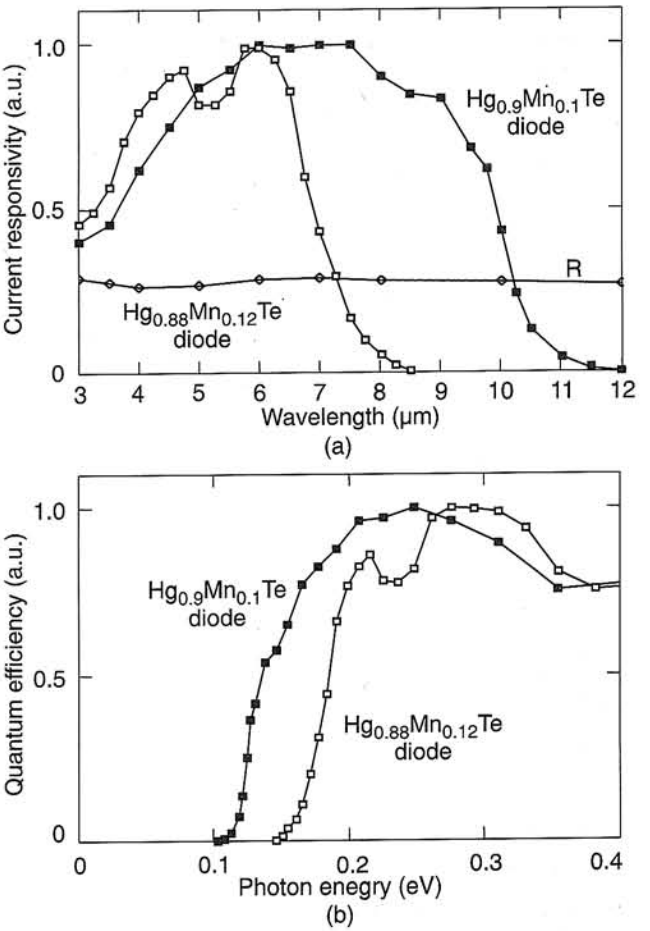

Fig. 6. Normalised dependence of photocurrent related to unit of radiation power as a function of wavelength (a), and related to one incident photon as a function of photon energy (b). The diamonds in Fig. 6(a) show the reflection coefficient measured for the $Hg_{0.9}Mn_{0.1}Te$ crystal.

The curves were taken at 80 K and zero bias, i.e., under conditions most commonly used for infrared photovoltaic detectors. The experimental data in Fig. 6(a) are presented as a dependence of photocurrent, I_{ph}, per unit of incident radiation power (A/W) versus wavelength λ (the so-called current responsivity). It can be seen that the long-wavelength edge (cutoff) for one of the samples corresponds to 10–11 μm, i.e., such a photodiode is suitable for operation in the atmosphere window 8–14 μm. Although its responsivity covers the 3–5 μm window the other diode with the cutoff wavelength 7–8 μm and obviously smaller dark current is more suitable for the 3–5 μm window (all other factors being the same).

Physically, the spectra for the diodes represented in Fig. 6(b) as a dependence of number of photogenerated electrons (~I_{ph}) per one incident photon versus photon energy, hν, are more informative. Indeed, in this case the cutoff at the *hν*-axis gives the energy approximately equal to the semiconductor bandgap (~0.11 and ~0.17 eV), and I_{ph}×hν versus hν curve represents the relative photoelectric quantum yield (quantum efficiency) of the diode. Nonuniformity in spectral responsivity in hν > E_g region

can be associated with the frequency dependence of the reflection coefficient from the crystal surface. However, the measurements show that the reflection coefficient R varies too weakly in this spectral range [see Fig. 6(a)], i.e., the observed shape of the spectral curves should be attributed to the photocurrent formation processes themselves.

We will treat the spectral distribution of the $Hg_{1-x}Mn_xTe$ diode quantum efficiency using the energy-band diagram of n^+-p junction and parameters found in the preceding sections. We will take into account generation of photocurrent in the front n^+-layer, p-type substrate, and in the depletion layer of the diode structure [see Fig. 7(a)]. To find the contributions of electron-hole pairs generated in these regions to the photocurrent, the diffusion equations with corresponding boundary conditions are usually solved (see for example [21,22]). In doing so, the electric field is assumed to act only in the depletion layer whereas in n^+- and p-region the field is nill (i.e., the carrier motion is respectively diffusion or drift in character). The concentration of excess holes, Δp, at the boundary between n^+-region and the depletion layer, as well as the concentration of excess electrons, Δn, at the boundary between p-region and the depletion layer, are accepted to be zero. At the front surface of the n^+-layer the boundary condition has a form $D_p d(\Delta p)/dx = S_p \Delta p$, while at the back surface of the substrate $D_n d(\Delta n)/dx = S_n \Delta n$. Here D_n and D_p are the diffusion coefficients of electrons and holes, respectively, S_p is the surface recombination velocity at the passivation layer/n^+-layer interface, and S_n is the recombination velocity at the back surface of the crystal.

Let's denote the thicknesses of junction, n^+- and p-regions by W_{pn}, W_n, and W_p [see Fig. 7(a)], and the diffusion lengths of electrons and holes by L_n and L_p, respectively. Then the number of electrons contributed to the photocurrent and elated to one incident photon (the so-called spectral response) as a result of photon absorption within the substrate (where electrons are minority carriers) can be written as [21]

$$\eta_n = \frac{\alpha L_n}{\alpha^2 L_n^2 - 1} e^{-\alpha (W_n + W_{pn})} \times \left\{ \alpha L_n - \frac{\frac{S_n L_n}{D_n}\left(\cosh \frac{W_p}{L_n} - e^{-\alpha W_p} \right) + \sinh \frac{W_p}{L_n} + \alpha L_n e^{-\alpha W_p}}{\frac{S_n L_n}{D_n} \sinh \frac{W_p}{L_n} + \cosh \frac{W_p}{L_n}} \right\}. \quad (12)$$

Since the substrate is rather thick (~1 mm), nonequilibrium carriers arise at the back surface only for small absorption coefficients. But then photoexcitation can be considered as almost uniform through the bulk, and therefore the surface recombination is of minor importance. Thus, the recombination at the back surface can be ignored and Eq. (12) is easily reduced to

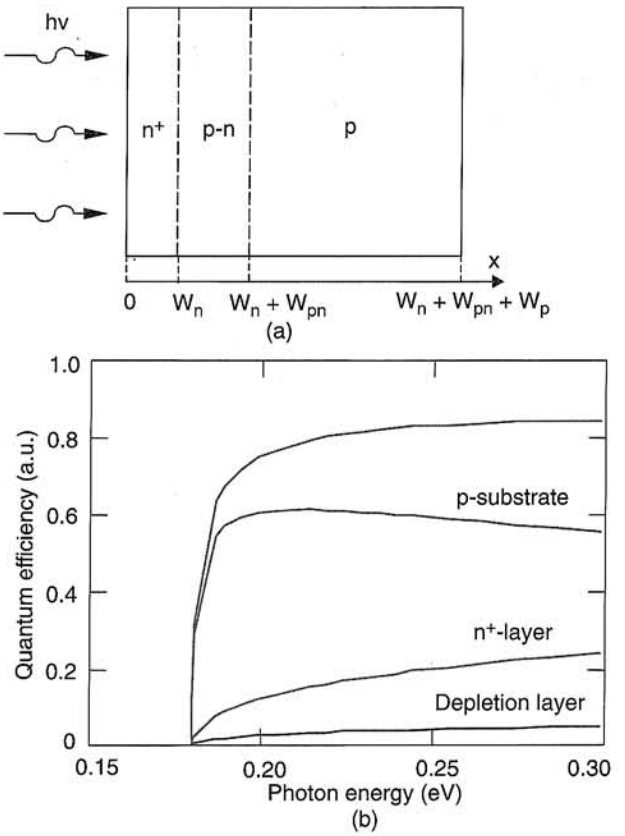

Fig. 7. Cross section of $Hg_{1-x}Mn_xTe$ photodiode (a), spectral response from p–n junction n^+- and p-regions (η_{pn}, η_n and η_p, respectively) (b). The top curve, η, shows the photodiode internal quantum yield.

$$\eta_n = \frac{\alpha L_n}{1 + \alpha L_n} \exp[-\alpha (W_n + W_{pn})], \quad (13)$$

where factor $\exp[-\alpha(W_n + W_{pn})]$ takes into account the optical absorption loss in n^+-layer and p–n junction.

The expression similar to Eq. (12) can be obtained for the spectral response from n^+-layer, i.e., for the hole contribution to the photoelectric efficiency

$$\eta_p = \frac{\alpha L_p}{\alpha^2 L_p^2 - 1} \times \left\{ \frac{\frac{S_p L_p}{D_p} + \alpha L_p - e^{-\alpha W_n}\left(\frac{S_p L_p}{D_p} \cosh \frac{W_n}{L_p} + \sinh \frac{W_n}{L_p} \right)}{\frac{S_p L_p}{D_p} \sinh \frac{W_n}{L_p} + \cosh \frac{W_n}{L_p}} - \alpha L_p e^{-\alpha W_n} \right\}, \quad (14)$$

but in this case the recombination at the front surface cannot be neglected.

The photocarriers generated within the depletion layer of the diode structure are swept out by electric field which prevents their recombination, and therefore the spectral response from the depletion layer is defined by [21]

 © 2000 COSiW SEP, Warsaw

$$\eta_{pn} = \exp(-\alpha W_n)[1 - \exp(-\alpha W_{pn})], \qquad (15)$$

where factor $\exp(-\alpha W_n)$ takes into account light absorption in n^+-layer. The spectral response from all the regions of the diode structure (the monochromatic quantum yield) is evidently given by the sum of three components

$$\eta(h\nu) = \eta_n(h\nu) + \eta_p(h\nu) + \eta_{pn}(h\nu). \qquad (16)$$

Obviously, the $\eta(h\nu)$ value is the monochromatic internal quantum yield. In order to obtain the external quantum yield, corrections for reflection at the front side of the photodiode and the optical absorption losses within the passivation layer must be made. Assuming the passivation layer to be transparent the external quantum yield can be found by multiplying $\eta(h\nu)$ by $(1 - R_{ef})$, where R_{ef} is the effective reflection coefficient for the passivation $Hg_{1-x}Mn_xTe$ surface. Note also that in order to go from the spectral distribution of quantum yield $\eta(h\nu)$ to the spectral distribution of current responsivity $I_{ph}(\lambda)$ one needs only divide $\eta(h\nu)$ by photon energy (expressed in eV).

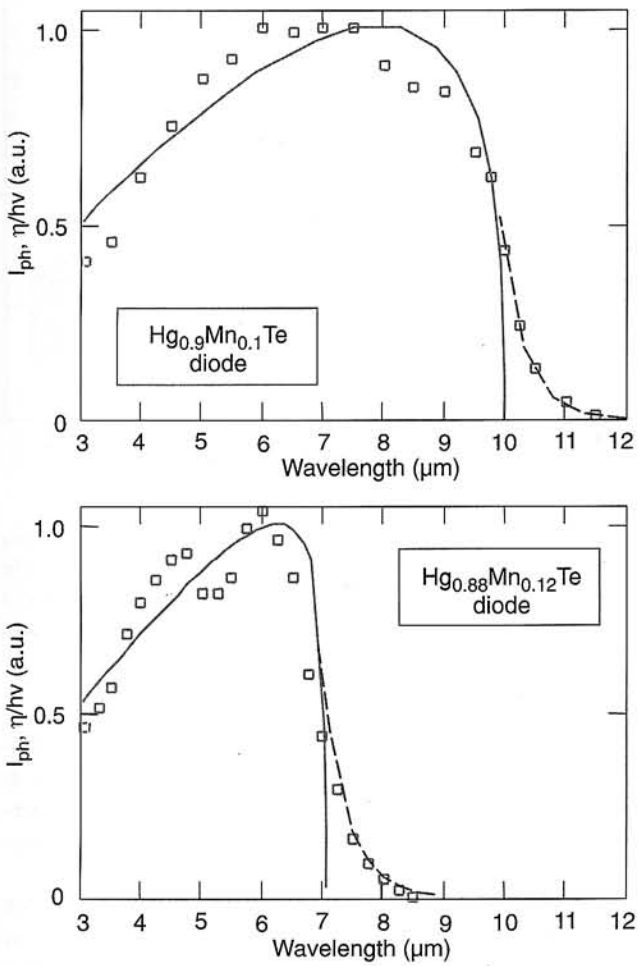

Fig. 8. Spectral current responsivity of the $Hg_{0.9}Mn_{0.1}Te$ and $Hg_{0.88}Mn_{0.12}Te$ photodiodes measured at 80 K (squares), calculated using Eqs. (13)–(16) (full lines) and with account made for broadening the absorption edge (dashed lines).

Assuming the photocurrent generated in $Hg_{1-x}Mn_xTe$ to be caused by interband electron transitions, for the absorption coefficient $\alpha(h\nu)$ appearing in Eqs. (12)–(15) one can use Eq. (4) for the $h\nu > E_g$ region and Eq. (7) for the tail of the absorption edge ($h\nu < E_g$). The dependence $\eta(h\nu)/h\nu$ computed using Eq. (16) for E_g = 0.1 and 0.17 eV are shown in Fig. 8(a) and (b) (normalised in maximum like the experimental curves). On calculating the following parameters were used: W_n = 1.5 μm, W_p = 0.8 mm, W_{pn} = 3×10^{-5} cm at V = 0. The values of D_n, D_p, L_n and L_p were found using relationships $eD_n/kT = \mu_n$ and $eD_p/kT = \mu_p$, $L_n = (D_n\tau_n)^{1/2}$ and $L_p = (D_p\tau_p)^{1/2}$; where μ_n and μ_p are the electron and hole mobilities taken equal to 10^5 $cm^2s^{-1}V^{-1}$ and 10^3 $cm^2s^{-1}V^{-1}$.

To gain the best fit to the observed spectra the electron lifetime in p-region, τ_n, was taken to be equal ~10^{-8} s, while the hole lifetime in n^+-region $\tau_p \approx 10^{-9}$ s. Such τ_n and τ_p values are significantly smaller than the effective lifetime of carriers in the depletion layer which lies within the range 10^{-5} to 10^{-6} s [23]. This "discrepancy" is due to the significant deference between carrier concentrations in different regions of the $Hg_{1-x}Mn_xTe$ diode structure: in the n^+-region the electron concentration is as large as ~10^{18} cm^{-3}, in the p–region of the $Hg_{1-x}Mn_xTe$ diodes the hole concentration is in excess of 10^{16} cm^{-3}, and in the depletion layer the free carriers can be neglected at all. As theoretical analysis shows [8,9,24], in a doped $Hg_{1-x}Mn_xTe$ like $Hg_{1-x}Cd_xTe$, the minority carrier lifetime decreases rapidly with the concentration of free carriers owing to increase in the probability of radiative interband recombination, and still further – of Auger recombination (in the latter case the recombination probability is proportional to n^2 and p^2, respectively).

It should be emphasised that the responsivity spectra of the $Hg_{1-x}Mn_xTe$ diodes is relatively insensitive to the surface recombination velocity at the front surface of the diode, S_p. One possible explanation for this is that the most part of carriers contributed to photocurrent is excited in p-region rather than n^+-region (even in the case of large absorption coefficients). This is illustrated in Fig. 7(b) where the spectral responses from n^+-layer, p-substrate and the depletion layer computed using Eqs. (13)–(15) are shown along with the photodiode total quantum yield. As is can be seen, even for $h\nu$ = 0.3 eV the spectral response by p-region (η_n) dominates the total diode photoresponse (η). Hence, effect of recombination at the front surface of n^+-layer can not be strong.

One can see from Fig. 8 that the calculated spectral responsivities for the $Hg_{1-x}Mn_xTe$ photodiodes reproduce the experimental curves only roughly. Notice first of all that for the calculated curves the responsivity goes considerably far into the $h\nu < E_g$ region. This is obviously because the absorption edge of $Hg_{1-x}Mn_xTe$ in $\alpha < 200$–300 cm^{-1} region has much gentle slope as compared to that predicted by theory (see Section 3). Therefore in the $h\nu < E_g$ region the photoresponsivity curves can be obtained from Eqs. (13)–(16) using Eq. (7). The results of calculation of the $Hg_{1-x}Mn_xTe$ diode responsivity thus performed for the re-

gion $h\nu < E_g$ is shown in Fig. 8 as dashed lines. It can be seen that the calculated "tails" and experimental data points are in close agreement.

As for the bulges and kinks observed in the responsivity spectra in the region $h\nu > E_g$ (at 4–6 μm and 7–9 μm in Figs. 7(a) and (b), respectively), one can explain them by the degeneracy of electron gas in n^+-layer of the diode structure (see Section 4). As already noted, such a degeneracy results in considerable entering the Fermi level into the conduction band and hence in the Burstein-Moss shift of the absorption edge. This means that the spectral response from n^+-layer comes into play not at $h\nu \geq E_g$ but at the photon energy greater than E_g by the Fermi energy E_{Fn}, i.e., at $h\nu \geq E_g + E_{Fn}$. In the region $E_g < h\nu < E_g + E_{Fn}$ photon-induced generation of electron-hole pairs in the n^+-layer is strongly attenuated.

6. Detectivity of the diodes

We will now turn to a key parameter of the $Hg_{1-x}Mn_xTe$ photodiodes such as their detectivity D^*. Let us begin with the R_oA product closely related to D^* (R_o is the zero bias differential resistance, and A is the area of the diode).

Figure 9(a) shows the voltage dependence of the differential resistance-area product RA = (dV/dI)A = (dV/dj) for two $Hg_{1-x}Mn_xTe$ diodes at 80 K. It can be see that for the $Hg_{0.9}Mn_{0.1}Te$ diode with cutoff wavelength λ_c = 10–11 μm the zero bias resistance-area product, R_oA, (i.e., the RA value at V = 0) is equal to 20–30 Ω cm^2 whereas for the $Hg_{0.9}Mn_{0.1}Te$ diode with λ_c = 7–8 μm $R_oA \approx 500$ Ω cm^2. A comparison with the data presented in a number of publications and collected in [24] shows, first of all, that the studied $Hg_{1-x}Mn_xTe$ photodiodes are competitive on this parameter with the $Hg_{1-x}Cd_xTe$ n^+-p photodiodes with the same values of λ_c. Next it is pertinent to compare the observed R_oA values with the theoretical dependence of R_oA on λ_c found from the conditions that thermal noise from resistance R_o is the same as the shot noise generated by background radiation, i.e., from the equality $4kT/R_oA = 2e^2\eta\phi_B$ (ϕ_B being the background photon flux density in the $\lambda \leq \lambda_c$ spectral region) [8,24]. Such a comparison indicates that the background radiation (rather than the low value R_oA caused by the conduction of the diode) governs the detectivity of $Hg_{1-x}Mn_xTe$ photodiodes. Indeed, the experimental R_oA values are really 1–2 orders of magnitude larger than the theoretically possible R_oA product for an ideal photovoltaic detector under background radiation 300 K, 2π FOV, η = 0.5. This in turn means that when cooling to ~80 K, the $Hg_{1-x}Mn_xTe$ diodes with λ_c = 10–11 μm and λ_c = 7–8 μm have detectivities D^* close to 5×10^{10} cmHz$^{1/2}$W^{-1} and $D^* \approx 10^{11}$ cmHz$^{1/2}$W^{-1}, respectively [8,24].

As to charge transport mechanism determining the observed R_oA value, electrical studies [23,25] lead to the assumption that the conduction of $Hg_{1-x}Mn_xTe$ diodes at low forward bias and hence the R_oA product are governed by carrier recombination in the depletion layer of the diode structure. This is evidenced by the presence of an

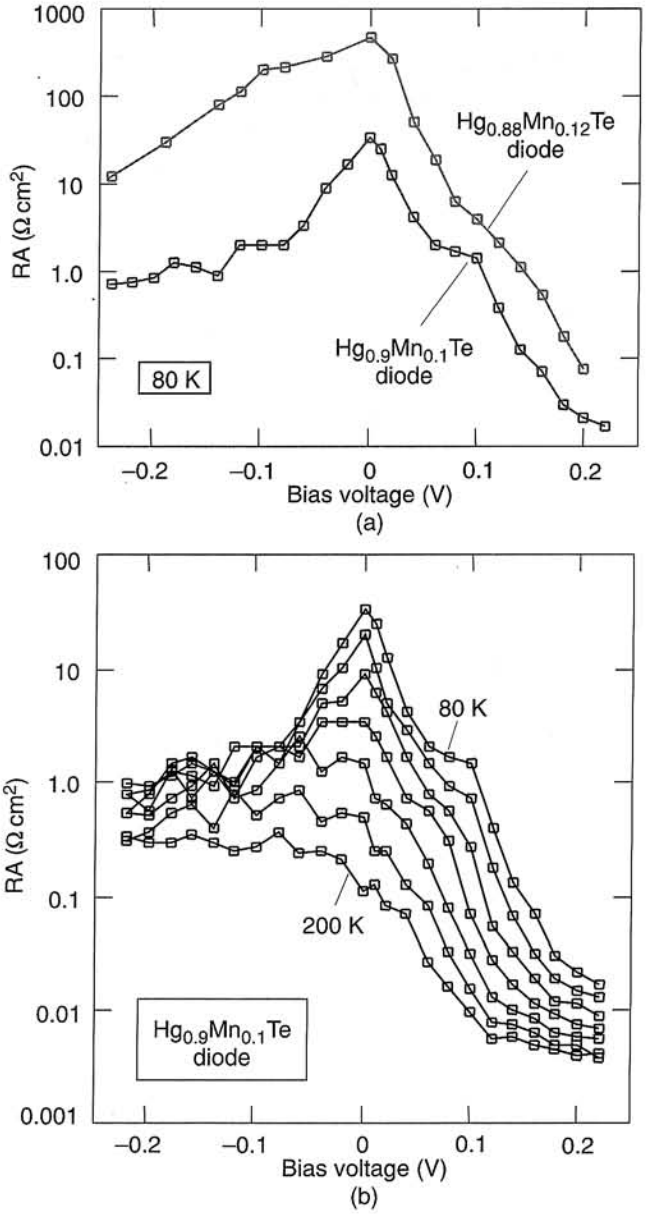

Fig. 9. Voltage dependence of the differential resistance-area product RA = (dV/dI)A for $Hg_{0.88}Mn_{0.12}Te$ and $Hg_{0.9}Mn_{0.1}Te$ diodes at 80 K (a) and for $Hg_{0.9}Mn_{0.1}Te$ diode at temperatures ranged from 80 K for the top curve to 200 K for the bottom curve in steps of 20 K (b).

I ~exp(eV/2kT) dependence in the forward I–V characteristic at low biases. Equally important is a drastic increase in forward current with temperature, which is easily understood bearing in mind that the recombination current is proportional to the intrinsic carrier concentration.

The assumption about recombination mechanism of the forward current is consistent with the temperature variation of differential resistance-area product RA for the diode presented in Fig. 9(b). As temperature elevates from 80 K to 200 K, the RA value in the low bias region decreases rapidly (about three orders of magnitude). It should be emphasised that at near-zero biases the temperature de-

 © 2000 COSiW SEP, Warsaw

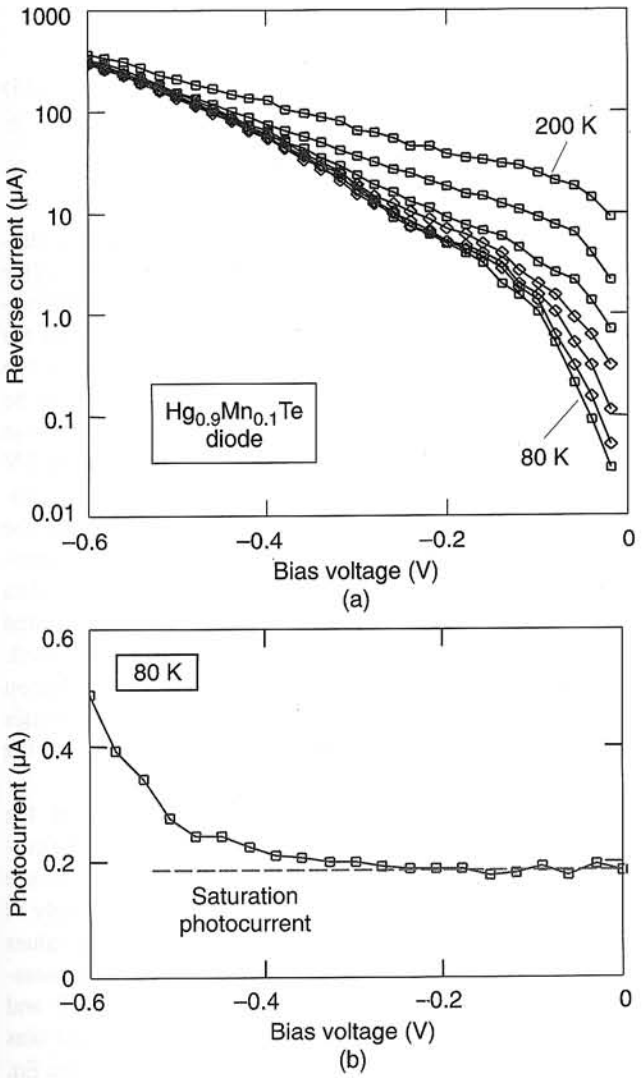

Fig. 10. Reverse current-voltage characteristics of $Hg_{0.9}Mn_{0.1}Te$ photodiode at different temperatures ranged from 80 to 200 K in steps of 20 K (a). Photocurrent generated by external radiation as a function of bias voltage (b).

pendence of the RA value at forward bias is slightly different from that at reverse bias. At higher reverse biases (> 0.15–0.2 V), however, the temperature dependence of the RA value reduces markedly: as temperature elevates within 80–200 K, the RA value at V = – 0.2 V decreases only about 3 times. One can suggest that the thermal generation current being prevalent at low reverse bias (< 0.1 V) is masked at higher bias by the current of another nature which depends only slightly on temperature.

In this connection the question araises as to the role of carrier tunnelling in charge transport and hence in determining the detectivity of the $Hg_{1-x}Mn_xTe$ photodiodes [25]. The results of temperature measurements presented in Figs. 10(a) and (b) seem to be highly informative in this respect. It is readily apparent from Fig. 10(a) that the reverse current involves at least two components. One of them strongly depends on temperature and therefore at higher temperatures dominates the current (in the low-bias region) whereas at liquid nitrogen temperatures it makes a negligible contribution to the charge transport. Notice next that I–V curves exhibit a well-defined kink at 0.25–0.3 V. The origin of the kink is revealed in the voltage dependence of the photocurrent, I_{ph}, generated by external infrared radiation. Figure 10(b) shows such a representative curve. The $I_{ph}(V)$ dependence is seen to be typical for a semiconductor photodiode. At low voltages, the $I_{ph}(V)$ curve exhibits a clearly delineated saturation where the I_{ph} value is close to the short-circuit photocurrent. When the voltage exceeds 0.25–3 V the saturation portion of the curve transforms into dependence with a considerable increase in the photocurrent with increasing V. The latter is known to be a direct evidence of impact ionisation and avalanche multiplication taken place in the diode. Assuming the multiplication of photocarriers and dark carriers to proceed in a similar way, one can conclude that the observed steeper increase of the reverse current at voltages higher than 0.25–0.3 V is due to impact ionisation of lattice atoms as well. At lower voltages, no impact ionisation occurs and the I–V dependence measured at low temperatures should be attributed to the tunnelling process. As already mentioned above, however, the differential resistance-area product RA depends sharply on T at V ≈ 0 not only under forward bias but also under reverse bias of the diode. The latter, however, seems not to be characteristic of the tunnelling process. In order to agree this discrepancy one is forced to assume that under reverse biases the tunnelling current decreases steeply when V→0 so that it becomes even smaller than the generation current.

When describing the tunnel current in the $Hg_{1-x}Mn_xTe$ or $Hg_{1-x}Cd_xTe$ diodes, the most frequently used approximation is that the tunnelling transitions occur in the region of p–n junction with maximum electric field. For an abrupt one-sided n^+-p junction the maximum field equal $2(\varphi_o\text{-}eV)/W$ [W being the depletion layer width defined by Eq. (11)] and then the reverse current caused by band-to-band tunnelling can be described by an expression of the form [21]

$$I = I_o \exp\left(-\frac{4}{3}\frac{\sqrt{m_r \varepsilon\varepsilon_o}}{\hbar N_a^{1/2}}\frac{E_g^{3/2}}{\sqrt{\varphi_o - eV}}\right), \qquad (17)$$

where I_o is the slowly varying function of V as compared to the exponential term

$$I_o = \frac{Ae^3}{2\pi^2\hbar^2}\left(\frac{m_r N_a}{\varepsilon\varepsilon_o\varphi_o E_g}\right)^{1/2} V(\varphi_o - eV)^{1/2}, \qquad (18)$$

m_r being the reduced electron and hole effective mass.

Our measurements show that the dependence given by Eq. (17) and the observed reverse I–V characteristics in the V < 0.3 V region (where carrier multiplication can be neglected) are normally diverged, with experimentally determined current always less than calculated. The cause of this discrepancy seems to arise from that the expression

(17) suggests to be applicable only for rather high reverse biases, namely for $|V| >> \varphi_o/e$, where tunnelling occurs near the top of the energy barrier. Furthermore, analysing the R_oA product, i.e., the diode differential resistance-area product at V = 0, the opposing electron flow must necessarily be taken into account. Indeed, although at V = 0 the measured current is equal to zero, the tunnelling process is not stopped: the electron transitions from n^+-region to p-region are balanced by the opposing transitions from p-region to n^+-region (as the eV value exceeds a few kT, the opposing flow can be neglected what is usually assumed when charge transport in $Hg_{1-x}Mn_xTe$ diodes is considered).

From the mentioned above, the more general expression for tunnelling current should be applied

$$I = I_{oo} \int_0^{\varphi_o - eV - E_g} \{[1 - f_n(E)]f_p(E) - [1 - f_p(E)]f_n(E)\}D(E)dE = I_{oo} \int_0^{\varphi_o - eV - E_g} \{f_p(E) - f_n(E)\}D(E)dE \quad (19)$$

where I_{oo} is the value coincident with I_o in Eq. (17) when $|eV| >> \varphi_o$, $f_n(E)$ and $f_p(E)$ are the probabilities for the level of the energy E to be occupied with an electron in n^+- and p-regions, respectively, D(E) is the tunnelling probability (the expression between the braces takes into account an opposing flow of electrons).

In the reference coordinate system where the origin of the E-axis is taken at the bottom of the conduction band in n^+-region (see Fig. 5)

$$f_n(E) = \left[\exp\left(\frac{E - E_F}{kT}\right) + 1\right]^{-1}, \qquad f_p(E) = \left[\exp\left(\frac{E - E_F + eV}{kT}\right) + 1\right]^{-1}, \quad (20)$$

and D(E,V) is defined in the WKB approximation as

$$D(E,V) = \exp\left(-\frac{2\sqrt{2m_r}}{\hbar}\int_{x_1}^{x_2}\sqrt{\varphi(x,V) - E}\,dx\right). \quad (21)$$

Here $\varphi(x,V)$ is the potential energy in the depletion layer given in the same coordinate system by

$$\varphi(x) = (\varphi_o - eV)\left[1 - \left(1 - \frac{x}{W_{pn}}\right)^2\right], \quad (22)$$

and x_1 and x_2 are the classical turning points determined by the equalities: $\varphi(x_1,V) - E = 0$ and $\varphi(x_2,V) - E = E_g$, i.e.,

$$x_1 = W_{pn}\left(1 - \sqrt{\frac{E + E_g}{\varphi_o - eV}}\right), \qquad x_2 = W_{pn}\left(1 - \sqrt{\frac{E}{\varphi_o - eV}}\right). \quad (23)$$

Figures 11(a) plots the voltage dependence of the tunnelling current calculated using Eqs. (19) and (17) (for comparison) for the $|V| < 0.25$ V bias region where the carrier multiplication is negligibly small. Also shown in the figure is the experimental data points taken for the $Hg_{1-x}Mn_xTe$ diode with $\lambda_c \approx 10$ μm at 80 K. As it can be seen, the curves calculated with Eqs. (17) and (19) diverge drastically when V→0 while at voltages larger than ~0.5 V the curves coincide. If Eq. (17) would be valid at low voltages, the calculated current will be much larger than the measured within the voltage region of interest. The expression (19) approximates more closely the experimental data than Eq. (17) does. However, as $|V| < 0.1$ V the measured current somewhat deviates upward from Eq. (19) as well. This supports our assumption about noticeable contribution of the generation current even at 80 K and hence provides an explanation for the observed strong dependence of the R_oA product on temperature.

Figure 11(b) shows the voltage dependence of the RA = (dV/dj) value for the $Hg_{0.9}Mn_{0.1}Te$ diode as the current is calculated using Eqs. (17) and (19). As one can see the RA value calculated using Eq. (19) increases steeply as V→0 becoming much larger than the experimental values (curve 1). As already mentioned, this is because the generation current masks the tunnelling current as V→0 and therefore the experimental points taken under reverse bias do not elevate along with the RA curve calculated from Eq. (19) but "meet" the points taken under forward bias.

Hence, at $V \approx 0$ the conduction of the $Hg_{1-x}Mn_xTe$ diodes studied is governed by generation-recombination of carriers rather than their tunnelling. It should be emphasised that the use of Eq. (17) for the tunnelling current leads to the opposite consequence. In this case the calculated R_oA product is about one order of magnitude smaller than obtained from the measurements (see Fig. 11(b), curve 2).

6. Conclusions

Multielement $Hg_{1-x}Mn_xTe$ (x = 0.1 and 0.12) photodiode arrays with p–n junction formed by ion etching have been fabricated. The rectifying and photovoltaic characteristics of the diodes are determined by p–n junctions with the strongly degenerate n^+-region and the barrier height of 0.24–0.27 eV, i.e., significantly larger than the semiconductor bandgap. At low forward and reverse biases the electrical properties of the diodes are governed by generation-recombination of carriers in the depletion layer. At higher reverse voltages the tunnelling mechanism domi-

 © 2000 COSiW SEP, Warsaw

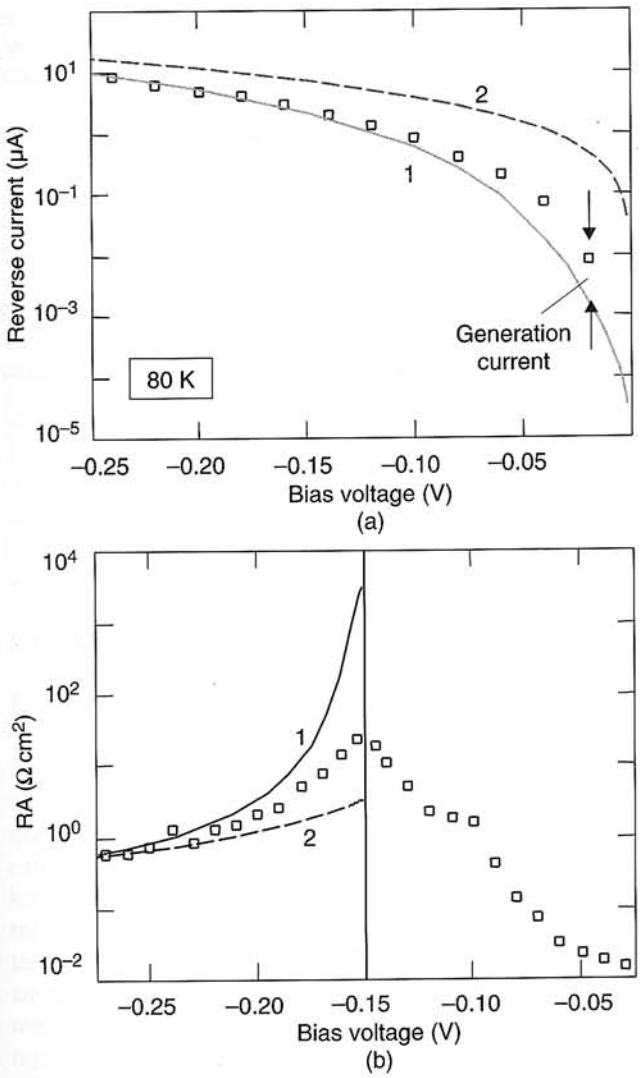

Fig. 11. Voltage dependence of reverse current (a) and differential resistance-area product (b) for $Hg_{0.9}Mn_{0.1}Te$ diode at 80 K. The points show experimental data, curves 1 and 2 correspond to the currents calculated using Eqs. (19) and (17), respectively.

nates charge transport with a further increase of the current due to impact ionisation of lattice atoms.

The intrinsic absorption of the $Hg_{1-x}Mn_xTe$ crystals is treated in the framework of the Kane theory with account made for the gentle sloping absorption edge due to compositional microfluctuations and inclusions in the material. The photoresponsivity of the $Hg_{1-x}Mn_xTe$ diodes is caused by electron-hole generation in n^+- and p-region as well as in p–n junctions. The zero bias resistivity-area product of the diodes (R_oA) is determined by generation-recombination in the depletion layer amounting up to 20–30 and ~500 $\Omega\,cm^2$ for the $Hg_{0.9}Mn_{0.1}Te$ and $Hg_{0.88}Mn_{0.12}Te$ diodes, respectively. The detectivity of the photodiodes is competitive to that of $Hg_{1-x}Cd_xTe$ photovoltaic detectors and limited by the background irradiation 300 K, 2π FOV.

Acknowledgements

The authors wish to express their thanks to Dr. V.M. Sklyarchuk for careful optical measurements, Mr Ma Dejun and Ms Guo Yunzi for technical assistance, and Mrs L.I. Khabailo for computer graphics and preparing manuscript of the paper.

References

1. R.T. Delves, "New galvanomagnetic effects in very small energy gap (HgMn)Te solid solutions", *Proc. Phys. Soc.* **87**, 809–824 (1966).
2. J.K. Furdyna, "$Hg_{1-x}Mn_xTe$: a new candidate for infrared detectors", *Proc. SPIE* **409**, 43–52 (1983).
3. A. Wall, C. Caprile, A. Franciosi, R. Reifenberger, and U. Debska, "New ternary semiconductors for infrared applications: $Hg_{1-x}Mn_xTe$", *J. Vac. Sci. Technol.* A **4**, 818–822 (1986).
4. P. Becla, "Infrared photovoltaic detectors utilising $Hg_{1-x}Mn_xTe$ and $Hg_{1-x}Cd_xTe$ alloys", *J. Vac. Sci. Technol.* A **4**, 2014–2018 (1986).
5. E. Janik and G. Karczewski, "Carrier transport mechanism in $Hg_{1-x}Mn_xTe$ photovoltaic diodes", *Acta Physica Polonia* A **73**, 439–442 (1988).
6. R. Triboulet, "Alternative small gap materials for IR detection", *Semicond. Sci. Techn.* **5**, 1073–1079 (1990).
7. P. Becla, S. Motakef, and T. Koehler, *J. Vac. Sci. Technol.* B **10**, 1599–1601 (1992).
8. A. Rogalski, "$Hg_{1-x}Mn_xTe$ as a new infrared detector material", *Infrared Phys.* **31**, 117–166 (1991).
9. A. Rogalski and J. Rutkowski, "The performance of $Hg_{1-x}Mn_xTe$ photodiodes", *Infrared Phys.* **29**, 887–893 (1989).
10. G. Bahir and E. Finkman, "Ion beam milling effect on electrical properties of $Hg_{1-x}Cd_xTe$", *J. Vac. Sci. Technol.* A **7**, 348–353 (1989).
11. P. Brogowski, H. Mucha, and J. Piotrowski, "Modification of mercury cadmium telluride, mercury manganese telluride and mercury zinc telluride", *Phys. Stat. Sol.* A **114**, K37–K40 (1989).
12. O.A. Bodnaruk, I.M. Gorbatyuk, S.E. Ostapov, and I.M. Rarenko, "Growth and structure perfection of cadmium-mercury and manganese-mercury chalcogenides", *Inorganic Materials* **31**, 1347–1351 (1995).
13. Sun Weiguo, L.A. Kosyachenko, and I.M. Rarenko, "Anodic fluoride on $Hg_{1-x}Mn_xTe$", *J. Vac. Sci. Technol.* A **15**, 2202–2206 (1997).
14. L.A. Kosyachenko, I.M. Rarenko, O.A. Bodnaruk, V.M. Frasunyak, V.M. Sklyarchuk, Y.F. Sklyarchuk, S. Weiguo, and L.Z. Xiong, "Characterisation of $Hg_{1-x}Mn_xTe$ single crystals and $Hg_{1-x}Mn_xTe$-based photodiodes", *Semicond. Phys. Quantum Electr. Opt.* **2**, 31–36 (1999).
15. E.O. Kane, "Band structure of indium antimonide", *J. Phys. Chem. Solids.* **1**, 249–261 (1957).
16. M.D. Blue, "Optical absorption in HgTe and HgCdTe", *Phys. Rev.* **134**, 227–234 (1964).
17. L.D. Saginov, V.P. Ponomarenko, V.A. Fedirko, and V.I. Stafeev, "Peculiarities of optical absorption in the edge of

the intrinsic absorption in narrow-gap $Cd_xHg_{1-x}Te$", *Fizika. Techn. Poluprov.* **16**, 470–473 (1982).

18. A.I. Vlasenko, Z.K. Vlasenko, and A.V. Ljubchenko, "Photoconductivity spectral characteristics of semiconductors with exponential fundamental absorption edge", *Semiconductors* **33**, 1171–1174 (1999).
19. G.L. Deftefanis, "Electrical doping of HgCdTe by ion implantation and heat treatment", *J. Crystal Growth* **86**, 700–722 (1988).
20. L.O. Budulac, "Defects, diffusion and activation in ion implanted HgCdTe", *J. Crystal Growth.* **86**, 723–734 (1988).
21. S.M. Sze, *Physics of Semiconductor Devices*, Ch. 14, Wiley, New York, 1981.
22. D.M. Brown, E.T. Downey, M. Ghezzo, J.W. Kretchner, R.J. Saia, Y.S. Liu, J.A. Edmond, G. Gati, J.M. Pimbley, and W.E. Schneider, "Silicon carbide UV photodiodes", *IEEE Trans. Electron Devices* **40**, 325–333 (1993).
23. L.A. Kosyachenko, I.M. Rarenko, O.A. Bodnaruk, and S. Weiguo, "Electrical properties of $Hg_{1-x}Mn_xTe$-based photodiodes", *Semiconductors* **33**, 1293–1296 (1999).
24. A. Rogalski, "Analysis of the A_oR product in n^+-p $Hg_{1-x}Cd_xTe$ photodiodes", *Infrared Phys.* **28**, 139–153 (1988).
25. L.A. Kosyachenko, I.M. Rarenko, S. Weiguo, and L.Z. Xiong, "Charge transport mechanisms in HgMnTe photodiodes with ion etched p–n junctions", *Solid-State Electron.* **44**, 1197–1202 (2000).

 © 2000 COSiW SEP, Warsaw